

# RSC Advances



This is an *Accepted Manuscript*, which has been through the Royal Society of Chemistry peer review process and has been accepted for publication.

*Accepted Manuscripts* are published online shortly after acceptance, before technical editing, formatting and proof reading. Using this free service, authors can make their results available to the community, in citable form, before we publish the edited article. This *Accepted Manuscript* will be replaced by the edited, formatted and paginated article as soon as this is available.

You can find more information about *Accepted Manuscripts* in the [Information for Authors](#).

Please note that technical editing may introduce minor changes to the text and/or graphics, which may alter content. The journal's standard [Terms & Conditions](#) and the [Ethical guidelines](#) still apply. In no event shall the Royal Society of Chemistry be held responsible for any errors or omissions in this *Accepted Manuscript* or any consequences arising from the use of any information it contains.

# One-pot synthesis affords perfectly six-fold symmetric Au microsnowflakes for excellent electrochemical biosensing and surface-enhanced raman scattering assay \*\*

Yan Zhang<sup>a</sup>, Yonghai Yue<sup>a</sup>, Yi Peng<sup>a</sup>, Chengcheng Huang<sup>a</sup>, Lidong Li<sup>a\*</sup>, Lin Guo<sup>a\*</sup>, Shihe Yang<sup>a,b\*</sup>

Received (in XXX, XXX) Xth XXXXXXXXXX 20XX, Accepted Xth XXXXXXXXXX 20XX  
DOI: 10.1039/b000000x

Herein, the Au microsnowflakes with six-fold symmetric branches were successfully synthesized. The morphological evolution and kinetics mechanism of this microstructure were well explained. By using this micromaterials, the fabricated biosensor shows excellent electrochemical performance in the range of 1 nM - 1 mM with the low detection limit of 352 pM toward adenosine. And it also provides excellent selectivity against other deoxyribonucleoside. Meanwhile, the Au microsnowflakes show good performance in surface enhanced raman scattering for the detection of p-mercapto benzoic acid (PMBA) molecules.

## 1. Introduction

In recent years, gold microparticles and nanoparticles have received a lot of attention in the field of electrochemical biosensing or surface-enhanced Raman scattering (SERS) due to their excellent biological compatibility, conducting capability, surface chemical activities and large specific surface areas.<sup>1</sup>

Aptamers are a kind of RNA and DNA molecules. They have great ability to bind with specific targets, thus they were isolated via SELEX from nucleic acids libraries.<sup>2,3</sup> To date, aptamers have been one of the most important candidates for molecular detection and disease diagnosis, due to their unique and specific advantages such as: convenience in screening, reproducibility during the synthesis and versatility in labeling<sup>4-7</sup>.

As an endogenous small molecule with potent vasodilator and antiarrhythmic activities, adenosine has stimulated a lot of scholars' interest. It plays a vital role in performing signaling functions in both the peripheral and central nervous system. In

the peripheral nervous system, adenosine is a powerful vasodilator in controlling of smooth muscle contraction and regulating cerebral.<sup>8</sup> In the central nervous system, adenosine performs extremely important neuroprotection during ischemia,<sup>9</sup> regulation of spinal motor pattern generation,<sup>10</sup> and induction of sleep.<sup>11</sup>

Because of the ability to equalize energy intake to metabolic demand in the 1980s, adenosine was named as "retaliatory metabolite" and obtained a great reputation.<sup>12</sup> Besides adenosine is the core of the cell's energy-containing compound, ATP. So the observation of adenosine fluctuations would be useful for further characterizing the role of it in brain function and behavior. Many scholars have reported lots of achievements in electrochemical analysis. For example, Lu's group developed a novel sensitive chemiluminescence (CL) aptasensor toward adenosine, which has the low detection limit of 80 nM.<sup>13</sup> Yu and co-workers reported a method to detect adenosine with the detection limit as low as 5 nM by using SERS<sup>14</sup> Lu's group have also developed a method to detect limited adenosine.<sup>15-16</sup> As we know that SERS has been greatly developed as a detection technique with great sensitivity since 1974. Uniform arrays with many little branches could drastically increase the ratio of total surface to volume.<sup>17</sup> As we know, the tips are generally considered as potential "hot spots" for localized near-field enhancements<sup>18</sup> and could potentially enhance the Raman scattering on the highly branched gold nanostructures. Tuan Vo-Dinh's group had synthesized gold nanostars with varying sizes, which can be used as a SERS substrate to detect p-mercapto benzoic acid (PMBA) with enhancement factor (EF)

of  $5 \times 10^3$ .<sup>19</sup> Meanwhile, in Guo Lin's group, tetrahedral (THH) and elongated tetrahedral (ETHH) gold nanocrystals (NCs) were introduced to experimentally investigate enhancement factors of SERS.<sup>20</sup> So the detection limit of adenosine may range differently due to the various Au nanostructures as SERS substrates.<sup>21-24</sup>

So far, various gold architectures have been widely achieved by different methods, it is still challenging to produce gold nanostructures with particular or complex structures. Dendritic nanostructures, which brought many potential applications in catalysis, biosensors and electronics,<sup>25</sup> have special textures, such as sharp edges or tips, nanoscale junctions and high surface areas. Wang and co-workers provides a pH-directed morphology control method to synthesize the morphology of five-star-like hierarchical gold nanostructures.<sup>26</sup> Chen and co-workers have reported that they had successfully synthesized 5-fold stellate polyhedral gold nanoparticles by using a seed-mediated growth method.<sup>27</sup> Zhang and co-workers reported the synthesis of platelet-like Au nanorods and six-star Au nanoparticles by photochemical reduction.<sup>28</sup> Tae Gwan Park and co-workers demonstrated a facile one-pot synthesis method to fabricate gold nanoparticles with diverse morphological characters by reducing precursor Au(III) ions into a gold crystal structure via a biphasic kinetically controlled reduction process.<sup>29</sup>

Though some gold architectures with 5 or 6 fold symmetry have been reported as above, the 6-fold symmetry of snowflake Au microparticles (AuMPs) is rarely reported, Such structure has some particular characteristic features as follows: 1. A single snowflake AuMP consists of a convex pistil, six convex pronounced petals with symmetric branches and some nanoparticles distributed on the center of the snowflake AuMPs. The large amount of regular edges, tips and the convex sections provide big surface area, thus enhance electrical conductivity of electrode for electrochemical biosensing and facilitate to provide greater enhancement for surface-enhanced Raman scattering (SERS). ; 2. The preparation method is convenient to be operated under the mild condition of 90 °C and a few parameters were involved. 3. The reaction is fast, economical and cheap with no expensive additives. Particularly environmental friendly AA and solvent water were used rather than strong sour, alkali or organic solvent.

Herein, we report a one-pot method to synthesize the particular morphology of gold snowflake microstructures. The

morphological evolution and kinetics mechanism were discussed in the article by being correlated with the growth model. Meanwhile, we developed an electrochemical biosensing method using gold snowflakes as substrate, which offered a significant improvement for adenosine detection with the low detection limit of 352 pM and obtained excellent surface-enhanced Raman scattering (SERS) sensitivity for detecting p-mercapto benzoic acid (PMBA) molecules.

## 2. Experimental Section

Hydrochloroauric acid tetrahydrate ( $\text{HAuCl}_4 \cdot 4\text{H}_2\text{O}$ ) was purchased from Shengyang jinke reagent works, cetyltrimethylammonium chloride (CTAC) purchased from Tianjin Jingke Fine Chemical Industry Research Institute was used as protecting agents, ascorbic acid (AA) obtained from Beijing Boaoxing Biological Technology Limited Liability Company was used as reducing, sodium bromide (NaBr) was supplied by Tianjin Jingke Fine Chemical Industry Research Institute.

All experiments were carried out in deionized water. 0.064g CTAC were dissolved in 20 mL water and mixed with NaBr (3.0 M, 700 uL) and AA (0.3 M, 0.5 mL). NaBr was used as structure-directing agent to help to acquire the selectively particular snowflake Au microstructure.<sup>30</sup> It had been reported that the specific adsorption of bromide ions in NaBr exerted major exquisite control over the shape evolutions by allowing distinct growth rates dependent on specific gold facets.<sup>31</sup> The CTAC that was assumed to have a micelle structure to be a major geometrical constraint, in fact, made a limited contribution to the crystal growth as an agent for the passive protection of the crystals.<sup>31</sup> During the experiment, we kept the flask in the oil of 90 °C for 15 minutes, and then we add the  $\text{HAuCl}_4$  solution ( $4 \times 10^{-4}$  M, 4 mL) dropwise. The reaction was finished after 90 minutes. The product will be washed three times by centrifugation (10000 rpm, 5 min).

Scanning electron microscopy (SEM) images were carried out with Quanta 250 FEG and JSM-7500F. High-resolution transmission electron microscopy (HRTEM) images were performed with a JEOL JEM-2100F microscope. The CHI 660C electrochemical workstation (Chenhua Instruments Co., Shanghai, China) was used for the electrochemical measurements. All experiments were performed using a conventional three-electrode system with a bare gold (diameter, 2 mm) as the working electrode, an Ag/AgCl as the reference

electrode and platinum as the counter electrode. All potentials were referred to the reference electrode. Raman spectra were recorded on a Jobin Yvon (Laboratory JY HR800) spectrometer employing a 633-nm laser line as the excitation source. The Raman band of a silicon wafer at  $520\text{ cm}^{-1}$  was used to calibrate the spectrometer. The spectra were obtained by using a  $50\times$  objective lens to focus the laser beam onto a spot with  $\sim 1.9\text{ }\mu\text{m}^2$ .

For the preparation of the adenosine biosensor, the gold electrode was firstly immersed in piranha solution (70%  $\text{H}_2\text{SO}_4$  (98%) and a mixture of 30%  $\text{H}_2\text{O}_2$  (30%)) for 10 min at room temperature. (CAUTION! Piranha reacts violently with organic solvents, and should be handled with extreme caution). Then, this electrode was rinsed with abundant amounts of water. Afterwards, the electrode was consecutively polished with 1.0, 0.3, and  $0.05\text{ }\mu\text{m}$  alumina slurry on a polishing pad. And then, the electrode was cleaned in the water for 2 min ultrasound. The cleaned electrode was subsequently voltammetrically cycled in 10 mM potassium ferricyanide solution until a representative cyclic voltammogram of clean gold electrode was obtained and then voltammetrically cycled in  $0.5\text{ M H}_2\text{SO}_4$  with the potential between  $-0.2$  and  $+1.6\text{ V}$  at  $100\text{ mV/s}$  to obtain the typical cyclic voltammogram. After that,  $20\text{ }\mu\text{L}$  of snowflake AuMCs (Au microcrystals) was dropped on the surface of the electrode. This modified electrode will be placed at the room temperature, dried in air and rinsed by deionized water then drop  $20\text{ }\mu\text{L}$  aptamers ( $1\text{ }\mu\text{M}$ , the amount of aptamers is  $2\times 10^{-11}\text{ mol}$ , contained tris (2-carboxyethyl) phosphine hydrochloride (TCEP) to reduce the disulfide bond and thus activate the thiolated aptamers) and kept at room temperature for another 16 hours. At last,  $20\text{ }\mu\text{L}$  6-Mercapto-1-hexanol (MCH) ( $10\text{ mM}$ ) was dropped on the above modified electrode to remove nonspecific aptamer adsorption and incubated at  $37\text{ }^\circ\text{C}$  for 1 hour, rinsed by deionized water and dried in  $\text{N}_2$ . Through these steps, snowflake AuMCs and aptamers was self-assembled on the surface of the gold electrode layer by layer. For the electrochemical measurement,  $20\text{ }\mu\text{L}$  of adenosine with various concentrations was dropped on the above modified gold electrode and incubate at  $37^\circ\text{C}$  in the incubator for 30 min and then rinsed by phosphate buffer (PBS) and deionized water successively.

The working electrode was immersed in the electrochemical cell containing 10 mL of  $0.2\text{ M PBS}$ ,  $10\text{ mM K}_4[\text{Fe}(\text{CN})_6]$ - $10\text{ mM K}_3[\text{Fe}(\text{CN})_6]$  ( $\text{pH}=7.0$ ). The electrochemical square-wave voltammetry measurements were carried out under the following conditions: The voltage scanned from  $0\text{ V}$  to  $0.6\text{ V}$

with a potential incremental of  $0.004\text{ V}$ , the amplitude, the frequency and the static time were kept as  $0.025\text{ V}$ ,  $25\text{ Hz}$ , and  $2\text{ s}$ , respectively.

The SERS substrate was prepared by dropping  $10\text{ }\mu\text{L}$  of the above-prepared sample onto a carefully cleaned silicon plate, which was allowed to dry naturally in air. The substrate was immersed into  $1\times 10^{-4}\text{ mol}\cdot\text{L}^{-1}$  p-mercapto benzoic acid (PMBA) ethanol solution and for 30 min. After drying at room temperature, it was then rinsed with deionized water and absolute ethanol several times to remove the free PMBA molecules.

### 3.Results and Discussion

**Figure 1** displays the typical SEM images of the snowflake-like Au microstructures. The low-magnification image in **Figure 1a** shows that the product consists of snowflake-like structures. The high-magnification image in **Figure 1b** shows the morphology of a single snowflake-like structure which consists of six pronounced petals with two symmetric sides of the branches. It can be seen that the six pronounced petals and the center of the snowflake Au microstructures are convex, and some nanoparticles distributed on the flower center. Furthermore, **Figure 1d**, **Figure 1e** and **Figure 1f** are the local magnified images of the snowflake-like Au microstructure as shown in **Figure 1c**, and the main part of snowflake morphology were well described by the three magnified figures.

The structure of the sample was further characterized by transmission electron microscopy (TEM). A snowflake-like morphology of an individual gold particle could be observed in **Figure 2a**. The high-resolution TEM (HRTEM) image of the snowflake Au microstructure is shown in **Figure 2b**. The clear lattice image indicates the high crystallinity of the snowflake-like gold microstructures. A lattice spacing of  $0.23\text{ nm}$  for the  $\{111\}$  planes can be readily resolved. **Figure 2c** shows a selected area electron diffraction (SAED) pattern of the single snowflake Au microstructure in **Figure 2a**. The hexagonal symmetry of these diffraction spots indicates that these snowflake Au microparticles are single crystals bounded mainly by  $\{111\}$  facets.<sup>32</sup> As shown in **Figure 2d**, five peaks corresponding to the  $\{111\}$ ,  $\{200\}$ ,  $\{220\}$ ,  $\{311\}$  and  $\{222\}$  planes for a face-centered cubic lattice of Au have been observed and the diffraction intensity ratio between  $\{200\}$  and  $\{111\}$  is lower than the conventional value ( $0.39$  vs  $0.52$ ).

Based on the observations we demonstrate that the prepared snowflake Au microstructure are dominated by many  $\{111\}$  facets, as a result the lower energy  $\{111\}$  planes tend to be preferentially oriented, which are parallel to the surface of the supporting substrate.

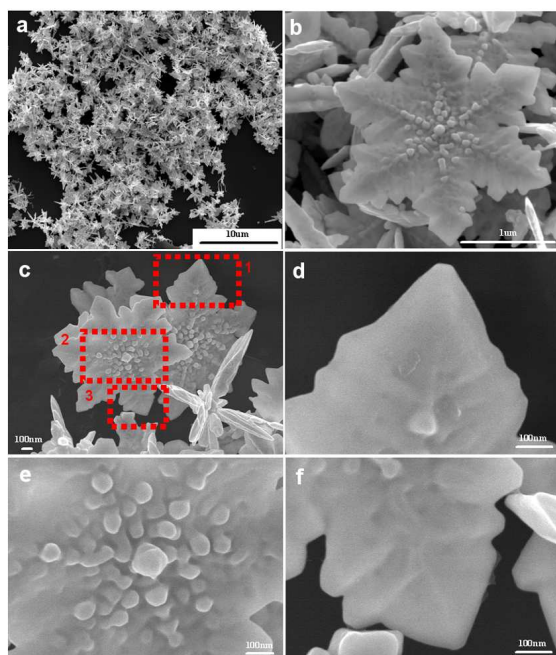


**Figure 1** SEM images of the as-prepared product at different magnifications: (a) low-magnification image of snowflake Au microstructures; (b) high-magnification image of a single snowflake Au microstructure; (c) part of snowflake Au microstructures; (d,e,f) local amplification images of (1,2,3) in Figure (c).

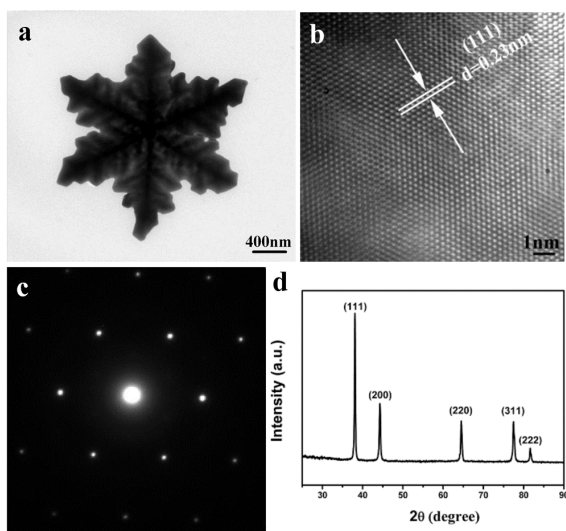


**Figure 2.** (a) TEM image of a single snowflake Au microstructure; (b) The HRTEM image of the snowflake Au microstructure; (c) SAED pattern from the single snowflake Au microstructure in (a) showing the hexagonal diffraction spot pattern indicative of the Au  $\{111\}$  facet; (d) XRD patterns obtained for the snowflake Au microstructures.

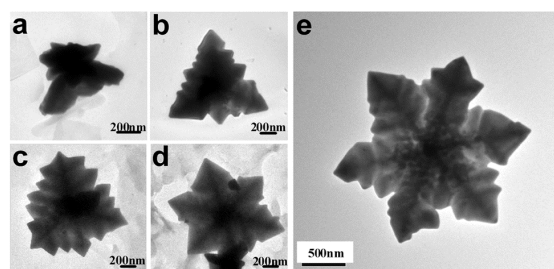


**Figure 3.** TEM images of snowflake gold microstructures obtained under different reaction times: (a) 5 s, (b) 30 s, (c) 4 min, (d) 10 min, and (e) 90min.

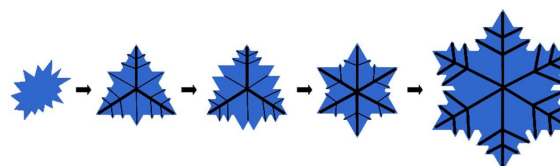


**Figure 4.** Schematic illustration of the proposed mechanism for snowflake Au microstructure.

While keeping the other reaction conditions constant, the formation process of the Au snowflakes in more details was revealed by the time dependent experiments, which were carried out at  $90^{\circ}\text{C}$  in the presence of CTAC with changing reaction times from 5s, 30s, 4min, 10min, up to 90min. The SEM images of the products, which were obtained at specific reaction time, are shown in **Figure 3**. Small nanoparticles were obtained at the first 5 s. The three pronounced petals with  $120^{\circ}$  in between, and a small amount of branches were obtained when the reaction time is shorter than 30 s. While another three pronounce petals grew a little on the symmetrically opposed direction. If the reaction time is prolonged to 4 min, the first three pronounced petals with more branches, and the latter three grown petals with small branches were obtained. We are surprised to find that the immature snowflake like Au microstructures appeared when the reaction time reached to 10 min. With the reaction time increases, the six pronounced petals grew longer with denser branches distributed on both sides of the petals, the perfect snowflake like AuMPs were completed at the end of 90 min. The schematic illustration of the Au snowflake microstructure formation process in aqueous solution is shown as **Figure 4**.

Some other control experiments were also performed as shown in **figure S1 - S6**. **Figure S1** shows that the morphology of as-prepared Au products without the addition of NaBr are irregular particles. As the above mentioned the specific adsorption of bromide ions in NaBr exerted major exquisite

control over the shape evolutions dependent on specific gold facets,<sup>31</sup> which also demonstrated by **figure S2**, in which NaCl was added instead of NaBr. When NaBr was replaced by KBr, the immature snowflake like Au microstructures appeared, the reason for this is that the cationic radius and interaction force between the cation and anion may both affect the morphology of Au crystal structure to be snowflake like Au microstructures. The different types of surfactant including cationic surfactant, anion surfactant and nonionic surfactant also lead to the different Au crystal morphologies as shown in **figure S3**. OTAC<sup>+</sup> and CTA<sup>+</sup> are different because of different chain length, the Au morphologies by using OTAC or CTAC are different. The differences between Br<sup>-</sup> and Cl<sup>-</sup> also made the great differences in Au morphology. The SEM images of as-prepared products when CTAB was directly used instead of CTAC/NaBr are shown in **figure S4**. It can be seen that the morphologies are changed from six-fold symmetric Au microsnowflakes to irregular particles. When the concentration of NaBr was kept at 3.0M, by using different concentrations of CTAC, the SEM images of the final product are shown in **Figure S5**. Based on the results from the **Figure S5**, when the CTAC concentration was kept at 0.01 M, the final product shows the perfect structure of six-fold symmetric Au microsnowflake. In **figure S6**, we kept changing NaBr concentrations, CTAC concentration was kept unchanged at 0.01 M. It can be seen that the microsnowflake structures disappeared when the concentration of NaBr was below 3.0 M. The specific adsorption of bromide ions in NaBr exerted major exquisite control over the shape evolutions by allowing distinct growth rates dependent on specific gold facets, whereas due to CTAC has a micelle structure to be a major geometrical constraint, CTAC made a limited contribution to the crystal growth as an agent for the passive protection of the crystals<sup>31</sup>.

As shown in **Figure 5**, there is an absorption peak at 980 nm for the Au microsnowflakes, and the SPR band is broadened in the near-infrared region for larger sized anisotropic gold microstructures. The Au microprisms were consisted of triangular, hexagonal and truncated triangular sheets with broad size range, so the Au microprisms could give a broad absorbance peak in UV-vis.

Herein, the electrochemical biosensing system for adenosine was studied as a model to investigate the electrochemical-sensing activity of snowflake AuMCs. As shown in **Figure 6**, in this design, the thiol-functionalized aptamers were immobilized on the snowflake AuMCs, which were modified on the gold

electrode surface via Au-S bond, while the other terminal of the aptamer is labeled with a ferrocene (Fc) group as the signal probe. In the absence of adenosine, the aptamer is in a free conformation, the distant positions between the Fc probe and working electrode surface is difficult for the electron transfer thus the background current is small. While in the presence of the adenosine, the aptamer partly bonded to the adenosine and folded to the complex structure. As a result, the efficiency of the electron transfer was increased between the redox Fc probe and the snowflake AuMCs modified gold electrode, significantly increasing the current intensity.

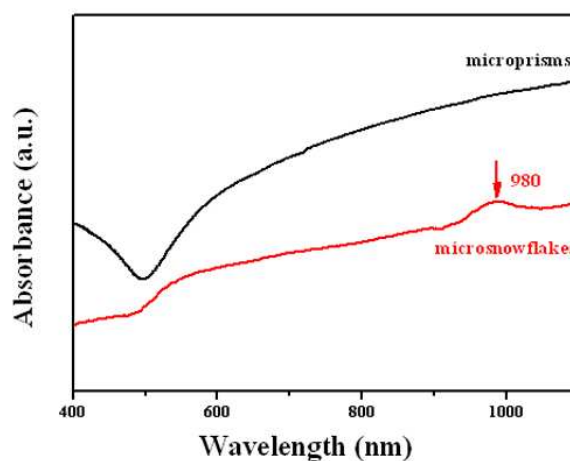


**Figure 5.** The UV-vis spectra of the Au microprisms and Au microsnowflakes.

Cyclic voltammogram (CV) was employed to describe the electrochemical properties of snowflake AuMCs and the data suggest an excellent performance compared with the bare electrode and prism AuMCs (as shown in **Figure S7**) modified electrode in this experiment. Figure 7 shows the enlarged total active surface area of working electrode modified by different AuNPs. The CV in 0.5 M H<sub>2</sub>SO<sub>4</sub> was used to measure the active surface areas at different Au electrodes. The gold oxide reduction was assumed to be required a specific charge of 386  $\mu\text{C}\cdot\text{cm}^{-2}$ .<sup>33</sup> The electrochemical active surface area (EASA) of the Au MPs can be estimated by  $\text{EASA} = Q_0/q_0$ , where  $Q_0$  is the surface charge obtained from the reduced area of gold oxide under the CV trace and  $q_0$  is the charge density accepted for the formation of one monolayer of gold oxide ( $q_0 = 386 \mu\text{C}\cdot\text{cm}^{-2}$ ).<sup>34</sup> Based on the calculation, we come to the conclusion that the total active surface area (10.16  $\text{mm}^2$ ) of the snowflake AuMCs/gold electrode is about 2.27-fold bigger than that (4.47  $\text{mm}^2$ ) of the electrode with prism AuMCs modification and 2.72-fold bigger than that (3.73  $\text{mm}^2$ ) of the bare electrode. Thus,

the total amount of anti-adenosine aptamers immobilized on snowflake AuMCs modified electrode surface is greater than that obtained from the prism AuMCs modified electrode and bare electrode.

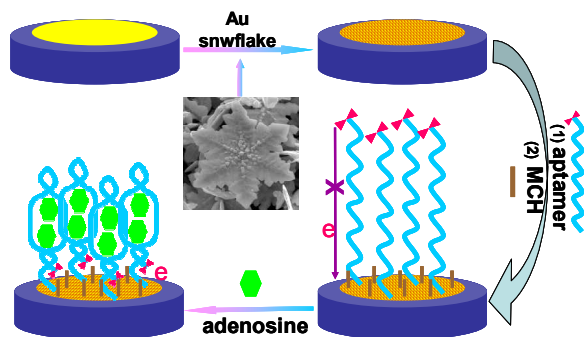


**Figure 6.** Adenosine-Responsive Sensing System and Experimental Principle.

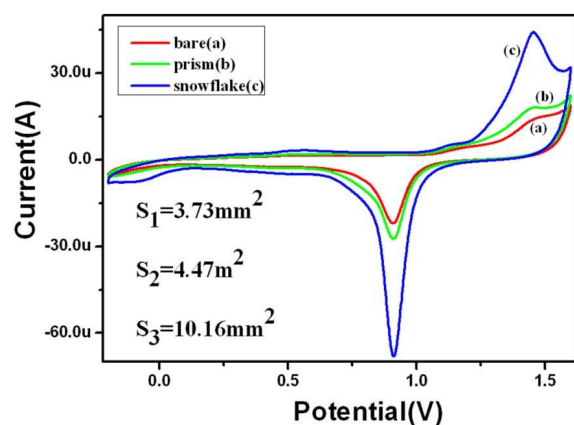


**Figure 7.** CVs of electrodes at scan rate of 100 mV/s: (a) a bare gold electrode, (b) prism AuMCs /gold electrode, (c) snowflake AuMCs /gold electrode.

In the further study, the electrochemical biosensing performance was tested by CV method in the PBS buffer after the well-prepared electrode reacted with adenosine solution in various concentrations. The results indicate that the aptamer and snowflake AuMCs based electrochemical biosensing system is highly sensitive to adenosine. **Figure 8a** displays the cyclic voltammetry curves for the aptamer / snowflake AuMCs / gold electrode after reacting with various concentrations of adenosine ranging from 1 nM to 1 mM. The CV curves indicate that the electrochemical current increased gradually with the increasing concentration of the adenosine. **Figure 8b** shows the dependence of the CV reduction peak current on various

adenosine concentrations (1 nM to 1 mM). Furthermore, the **Figure 8b** inset suggests that the reduction peak current is linearly related to the logarithm of the different concentration of adenosine from 1 nM to 1 mM. The regression equation is  $I = 5.86 \times 10^{-7} + 2.486 \times 10^{-8} \log C$  (unit of  $C$ , mol/L) and the regression coefficient ( $R$ ) is 0.995. The low limit detection of the proposed electrochemical biosensing strategy was thought to be 352 pM compared with other previously published methods<sup>15,16</sup> and we thought the following reasons contributed to the high sensitivity. First of all, the surface of a gold electrode was modified by snowflake AuMCs with more accidented surfaces, which contained six pronounced petals, center of the snowflake Au microstructures and some nanoparticles distributed around the pistil. This larger specific surface area thus greatly enhanced the immobilization amount of the thiol-functionalized aptamer. Additionally, the design of the electrochemical biosensing system introduced the ferrocene label which did not need a complex procedure described by the previous researchers<sup>5</sup> thus simplified the detection procedure at a large scale, and the simplification also improved the accuracy for the detection as other additives are not needed.

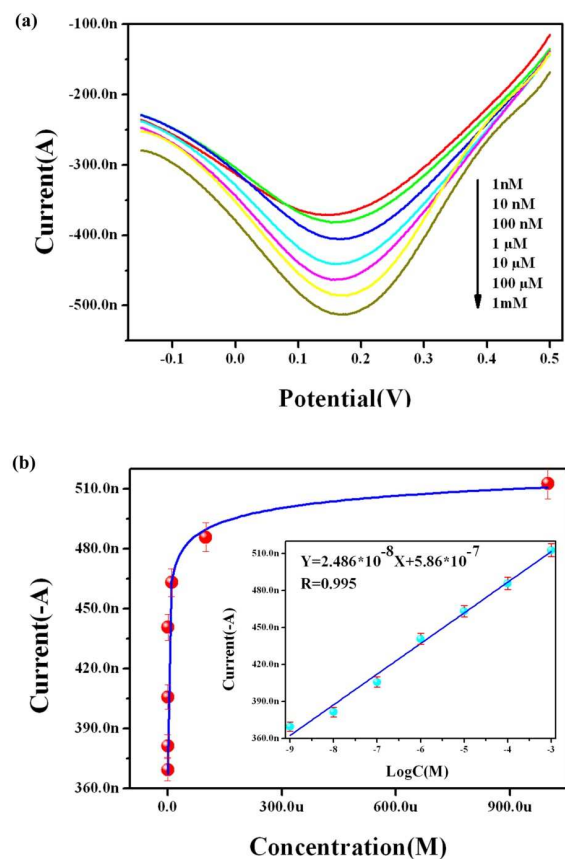


**Figure 8.** (a) Square-wave voltammograms of sensing system to different concentrations of adenosine of (1) 1 nM, (2) 10 nM, (3) 100 nM, (4) 1  $\mu$ M, (5) 10  $\mu$ M, (6) 100  $\mu$ M, (7) 1 mM in (a); (b) The signal

increase in the SWV as a function of adenosine concentration. Inset: the SWV peak current is linear with logarithm of adenosine concentration over the range from 1 nM to 1 mM; Inset: the CV peak current is linear with the logarithm of adenosine concentration ( $\log C(M)$ ) from 1 nM to 1 mM. The illustrated error bars represent the standard deviation of three measurements conducted with a single electrode at each concentration.

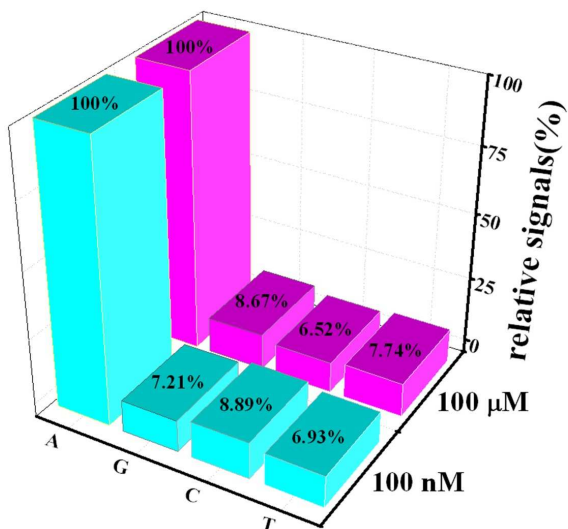


**Figure 9.** Relative response of the system to the different deoxyribonucleoside.

The selectivity of the biosensing system was determined by challenging it with the other three types of deoxyribonucleoside such as guanosine, cytidine and thymidine at 100 nM and 100 μM concentrations. As shown in **Figure 9**, the relative responses for the other deoxyribonucleosides are only as small as the background (in the absence of any deoxyribonucleosides) compared with the samples when using 1 μM or 100 nM adenosine. And the calculated data show that relative response of the guanosine, cytidine and thymidine are below 10%. This excellent selectivity arises from the high specificity of anti-adenosine aptamers.

Since the discovery of the SERS technique in 1974, it has been well designed and fabricated<sup>35</sup> and becomes a powerful tool for molecule detection, sensor application, surface process study as a branch of Raman spectroscopy and an important characterization tool in nanoscience study.<sup>36</sup> The SERS substrates with regular arrays, stable, uniform over relatively large areas are more promising candidates for investigations.<sup>37</sup>

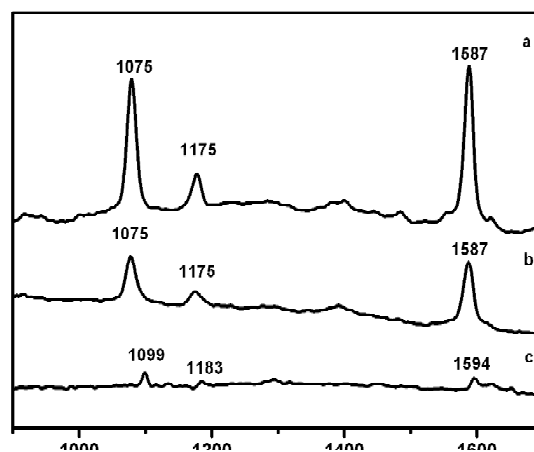


**Figure 10.** Raman and SERS spectra: (a) SERS spectra of PMBA adsorbed on Au microsnowflakes; (b) SERS spectra of PMBA adsorbed on Au microprisms; (c) Raman spectra of solid PMBA. All of the spectra reported were the result of 10s accumulation.

Herein, the SERS activity of as-prepared Au microsnowflakes and the microprisms were investigated and the PMBA was selected as the probe molecule.<sup>20</sup> The normal Raman spectra of solid PMBA and the SERS spectra of PMBA adsorbed on the microsnowflakes and microprisms of Au excited with the 647 nm laser line are presented in **Figure 10**. Compared with normal Raman spectrum of solid PMBA shown in **Figure 10 (c)**, we find that the Raman shift was changed and the Raman intensity was enhanced in the SERS spectra on the two different Au substrates. As shown in **Figure 10**, the predominant bands in the spectrum of solid PMBA are located at 1099, 1183 and 1594  $\text{cm}^{-1}$ , which are assigned to  $\nu_{\text{CS}}$ ,  $\delta_{\text{CH}}$ , and  $\nu_{\text{CC}}$ , respectively. In SERS spectrum, the band  $\nu_{\text{CS}}$  shifted from 1099  $\text{cm}^{-1}$  to 1075 because of the formation of Au-S bonding.<sup>20</sup> The  $\nu_{\text{CC}}$  band at 1594  $\text{cm}^{-1}$  shifted to 1587 and the  $\delta_{\text{CH}}$  band shifted from 1183  $\text{cm}^{-1}$  to 1175 as a result of bonding and electronic structure changes. As we see that the SERS intensity on a snowflake Au microstructures substrate gains nearly more than twice enhancement than that of on a prism Au microstructures substrate. Particularly, the SERS intensities of the  $\nu_{\text{CS}}$  mode at 1075  $\text{cm}^{-1}$  and  $\nu_{\text{CC}}$  band at 1587  $\text{cm}^{-1}$  the snowflake Au microstructures substrate gain greater enhancement than prism Au microstructures substrate. This result suggests that the snowflake Au microstructures could be used as an ideal active SERS substrate.

#### Enhancement Factors.

It is generally considered that the enhancement of a1 mode in SERS mainly originated from EM mechanism. To evaluate the enhancement activity more quantitatively, two predominant a1 bands discussed earlier in the paper were selected to

determine the enhancement factor (EF) according to the following equation:<sup>18,38</sup>

$$EF = \frac{I_{\text{SERS}}/N_{\text{ads}}}{I_{\text{bulk}}/N_{\text{bulk}}} \quad (1)$$

In eq 1,  $I_{\text{SERS}}$  and  $I_{\text{bulk}}$  are the measured vibration intensity in the SERS and normal Raman spectra, respectively.  $N_{\text{bulk}}$  and  $N_{\text{ads}}$  are the molecule number of solid and adsorbed PMBA in the laser illumination volume, respectively. And  $N_{\text{bulk}}$  was acquired via eq 2:

$$N_{\text{bulk}} = Ahn_{\text{bulk}} = Ah \frac{\rho_{\text{bulk}}}{M_{\text{bulk}}} N_A \quad (2)$$

The illuminated volume was calculated as the product of the area of the laser spot  $A$  ( $\sim 1.9 \mu\text{m}^2$ ) and the penetration depth  $h$  of the focused laser ( $\sim 15.4 \mu\text{m}$ ). Considering the density ( $1.49 \text{ g/cm}^3$ ) of bulk PMBA,  $N_{\text{bulk}}$  was calculated as  $1.7 \times 10^{11}$ . As for SERS samples,  $N_{\text{SERS}}$  could be obtained via eq 3:

$$N_{\text{SERS}} = \frac{AN_{\text{sub}}A_{\text{sub}}}{\sigma} \quad (3)$$

$A$  is the area of the focal laser spot ( $\sim 1.9 \mu\text{m}^2$ ).  $A_{\text{sub}}$  is the occupied area of individual microparticle ( $\sim 1.4 \mu\text{m}^2$ ) and  $\sigma$  represents the surface area occupied by one adsorbed PMBA molecule about  $0.3 \text{ nm}^2$  according to the literature.<sup>39</sup> Assuming that a layer of Au nanoparticles deposited on the substrate homogeneously, number density of Au NPs ( $N_{\text{sub}}$ ) could be counted from the SEM figure. According to the parameters above,  $N_{\text{SERS}}$  was finally estimated as  $6.2 \times 10^6$  and  $2.5 \times 10^6$  for Au microsnowflakes and microprisms samples, respectively.

By substituting the values of the variables into eq 1, enhancement factor (EF) of PMBA adsorbed on Au microsnowflakes and microparisms was estimated to be about  $3.2 \times 10^5$  and  $3.0 \times 10^5$ , respectively. Based on above results, an enhancement factor of  $10^5 \sim 10^6$  that was mainly contributed by electromagnetic mechanism was finally estimated.

As we know that a few molecules adsorbed on hot sites<sup>40</sup> contributed a most part in the strength of SERS spectrum.<sup>41</sup> Tips or edges on coin metal microstructures are generally considered to be of the huge enhancement.<sup>20</sup> As a result, the regular convex petals and pistils with the branches presented in the snowflake AuMPs, which cause larger roughness on the surfaces to be inclined to produce more hot spots, facilitated to provide greater enhancement than the prism AuMPs.

## Conclusion

In summary, a peculiar 6-fold symmetric Au microcrystals with convex flower pistil and six pronounced petals were successfully synthesized through one-pot synthesis method which was convenient, fast, economical and green environmental. The excellent performance of electrochemical sensing toward adenosine was obtained with a low detection limit of  $352 \text{ pM}$ . The unique morphology of Au microstructure can assist electrochemical biosensing to exhibit excellent sensitivity towards its target molecules and provide a promising platform for more aptamer immobilization for capture. The morphological evolution and kinetics mechanism were well explained by morphological changes at different reaction times in a qualitative manner to predict the growth mechanism of the six-fold gold structures. Besides, the unique morphology of gold microstructures also demonstrates the outstanding performance of SERS which implied the Au microsnowflakes could be used as substrates in some applications such as electronics, catalysis, and imaging.

**Acknowledgment.** This work was financially supported by the National Basic Research Program of China (2010CB934700), the National Natural Science Foundation of China (51272012, 51302208, 21273001) and Specialized Research Fund for the Doctoral Program of Higher Education (20111102130006).

<sup>a</sup> School of Chemistry and Environment, Beihang University, Beijing 100191, PR China. lilidong@buaa.edu.cn; guolin@buaa.edu.cn

<sup>b</sup> Department of Chemistry, The Hongkong University of Science and Technology, Clear Water Bay, Kowloon, HongKong, China

† Electronic Supplementary Information (ESI) available: details of any supplementary information available should be included here]. See DOI: 10.1039/b000000x/

## Reference

1. S. Guo, E. Wang, *Anal. Chim. Acta.*, 2007, **598**, 181-192.
2. A. D. Ellington and J. W. Szostak, *Nature*, 1990, **346**, 818-822.
3. C. Tuerk and L. Gold, *Science*, 1990, **249**, 505-510.
4. Stojanovic, M.N., de Prada, P., Landry, D.W., *J. Am. Chem. Soc.*, 2001, **123**, 4928-4931.
5. Chenhu Suna, Xueping Liua, Kejun Fengb, Jianhui Jianga, Guoli Shena, Ruqin Yu, *Analytica Chimica Acta*, 2010, **669**, 87-93.
6. Bang, G.S., Cho, S.Y., Kim, B.G., *Biosens. Bioelectron.*, 2005, **21**, 863-870.
7. Baker, B.R., Lai, R.Y., Wood, M.S., Doctor, E.H., Heeger, A.J., Plaxco, K.W., *J. Am. Chem. Soc.*, 2006,

- 128**, 3138–3139.
8. Maria Portellos, Charles E. Riva, Stephen D. Cranstoun, Benno L. Petrig, and Alexander J. Brucker, *Investigative Ophthalmology & Visual Science*, 1995, **36**, 1904-1909.
  9. N. Dale, T. Pearson, B. G. Frenguelli, *Journal of Physiology*, 2000, **526**, 143-155.
  10. N. Dale; D. Gilday, *Nature*, 1996, **383**, 259-263.
  11. T. Porkka-Heiskanen, *Ann. Med.*, 1999, **31**, 125-129.
  12. Andrew C. Newby, *Trends Biol. Sci.*, 1984, **9**, 42-44.
  13. Xiluan Yana, Zhijuan Caoa, Masaaki Kaib, Jianzhong Lu, *Talanta*, 2009, **79**, 383-387.
  14. J.-W. Chen, X.-P. Liu, K.-J. Feng, Y. Liang, J.-H. Jiang, G.-L. Shen, R.-Q. Yu, *Biosensors and Bioelectronics*, 2008, **24**, 66-71.
  15. Juewen Liu, Debapriya Mazumdar, Yi Lu, *Angew. Chem.*, 2006, **118**, 8123-8127.
  16. Juewen Liu, Yi Lu, *Angew. Chem.*, 2006, **118**, 96-100.
  17. J. Grand, M. Lamy de la Chapelle, J. L. Bijeon, P. M. Adam, A. Vial, P. Royer, *Phys. Rev. B*, 2005, **72**, 033407.
  18. Jixiang Fang, Shuya Du, Sergei Lebedkin, Zhiyuan Li, Robert Kruk, Manfred Kappes, Horst Hahn, *Nano Lett.*, 2010, **10**, 5006–5013.
  19. Christopher G. Houry, Tuan Vo-Dinh, *J. Phys. Chem. C*, 2008, **112**, 18849–18859.
  20. Peng-Gang Yin, Ting-Ting You, En-Zhong Tan, Jing Li, Xiu-Feng Lang, Li Jiang, Lin Guo, *J. Phys. Chem. C*, 2011, **115**, 18061-18069.
  21. Fan Li, Juan Zhang, Xuni Cao, Lihua Wang, Di Li, Shiping Song, Bangce Ye and Chunhai Fan, *Analyst*, 2009, **134**, 1355–1360.
  22. Shusheng Zhang, Jianping Xia, and Xuemei Li, *Anal. Chem.*, 2008, **80**, 8382–8388.
  23. Karuppuchamy Selvaprakash, Yu-Chie Chen, *Biosensors and Bioelectronics*, 2014, **61**, 88–94.
  24. Fu-Hsiang Ko and Yu-Cheng Chan, *RSC Adv.*, 2014, **4**, 26251–26257.
  25. (a) A. Mohanty, N. Garg, R. C. Jin, *Angew. Chem.*, 2010, **122**, 5082-5086. (b) M. Yang, R. Alvarez-Puebla, K. Hyoung-Sug, P. Aldeanueva-Potel, L. M. Liz-Marzan, N. A. Kotov, *Nano Lett.*, 2010, **10**, 4013-4019.
  26. Zidong Wang, Madurai Srinivasan Bharathi, Ramanarayan Hariharaputran, Hang Xing, Longhua Tang, Jinghong Li, Yong-Wei Zhang, and Yi Lu, *ACS NANO*, 2013, **7**, 2258-2265.
  27. Lin Jiang, Yuxin Tang, Chihao Liow, Jinsong Wu, Yinghui Sun, Yueyue Jiang, Zhili Dong, Shuzhou Li, Vinayak P. Dravid, and Xiaodong Chen, *Small*, 2013, **9**, 705-710.
  28. Xiao Huang, Xiaoying Qi, Yizhong Huang, Shaozhou Li, Can Xue, Chee Lip Gan, Freddy Boey, and Hua Zhang, *ACS NANO*, 2010, **4**, 6196-6202.
  29. Yuhan Lee, Tae Gwan Park, *Langmuir*, 2011, **27**, 2965–2971.
  30. Joseph S. DuChene, Wenxin Niu, John M. Abendroth, Qi Sun, Wenbo Zhao, Fengwei Huo, and W. David Wei, *Chem. Mater.*, 2013, **25**, 1392-1399.
  31. Tai Hwan Ha, Hee-Joon Koo, Bong Hyun Chung, *J. Phys. Chem. C*, 2007, **111**, 1123-1130.
  32. Z. L. Wang, *J. Phys. Chem. B*, 2000, **104**, 1153-1175.
  33. R. Szamocki, A. Velichko, C. Holzapfel, F. Mücklich, S. Ravaine, P. Garrigue, N. Sojic, R. Hempelmann, A. Kuhn, *Analytical chemistry*, 2007, **79**, 533-539.
  34. G. Tremiliosi-Filho, L.H. Dall’Antonia, G. Jerkiewicz, *Journal of Electroanalytical Chemistry*, 2005, **578**, 1–8.
  35. K. B. Li, L. Clime, L. L. Tay, B. Cui, M. Geissler, T. Veres, *Anal. Chem.*, 2008, **80**, 4945-4950.
  36. Hong Wei, Feng Hao, Yingzhou Huang, Wenzhong Wang, Peter Nordlander, and Hongxing Xu, *Nano Lett.*, 2008, **8**, 2497–2502.
  37. J. Grand, Lamy de la Chapelle, J.-L. Bijeon, P.-M. Adam, A. Vial, and P. Royer, *Phys. Rev. B*, 2005, **72**, 0334077.
  38. Y. L. Wang, X. Q. Zou, W. Ren, W. D. Wang, E. K. Wang, *J. Phys. Chem. C*, 2007, **111**, 3259-3265.
  39. L. X. Xia, H. B. Wang, J. Wang, K. Gong, Y. Jia, H. L. Zhang, M. T. Sun, *J. Chem. Phys.*, 2008, **129**, 134703.
  40. Jixiang Fang, Shuya Du, Sergei Lebedkin, Zhiyuan Li, Robert Kruk, Manfred Kappes, and Horst Hahn, *Nano Lett.*, 2010, **10**, 5006-5013.
  41. Ying Fang, Nak-Hyun Seong, Dana D. Dlott, *Science*, 2008, **321**, 388-393.

